Journal of Physics: Conference Series **488** (2014) 012036 doi:10.1088/1742-6596/488/1/012036

Surface-morphology changes and damage in hot tungsten by impact of 80 eV - 12 keV He-ions and keV-energy self-atoms

F W Meyer[1*], P S Krstic[2,3], H Hijazi[1], M E Bannister[1], J Dadras[2], C M Parish[4], and H M Meyer III[4]

[1]Physics Division, Oak Ridge National Laboratory, Oak Ridge, TN 37831-6372 USA

[2]University of Tennessee, Knoxville, TN 37831-6173 USA

[3]TheoretiK, Knoxville, TN 37921 USA

[4]Materials Science and Technology Division, Oak Ridge National Laboratory, Oak Ridge, TN 37831-6064 USA

[*]E-mail: meyerfw@ornl.gov

Abstract. We report results of measurements on the evolution of the surface morphology of a hot tungsten surface due to impacting low-energy (80 – 12,000 eV) He ions, performed at the ORNL Multicharged Ion Research Facility (MIRF). Surface-morphology changes were investigated over a broad range of fluences, energies and temperatures for both virgin and pre-damaged W-targets. At low fluences, ordered coral-like and ridge-like surface structures are observed, with great grain-to-grain variability. At the largest fluences, individual grain characteristics disappear in FIB/SEM scans, and the entire surface is covered by a multitude of near-surface bubbles with a broad range of sizes, and disordered whisker growth, while in top-down SEM imaging the surface is virtually indistinguishable from the nanofuzz produced on linear plasma devices. These features are evident at progressively lower fluences as the He-ion energy is increased. In addition, simulations were carried out of damage caused by cumulative bombardment of 1 keV W self-atoms, using LAMMPS at the Kraken supercomputing facility of the University of Tennessee. The simulations show strong defect-recombination effects that lead to a saturation of the total defect number after a few hundred impacts, while sputtering and implantation lead to an imbalance of the vacancy and interstitial numbers.

1. Introduction

Because of its high melting point, excellent erosion resistance, and excellent material strength, tungsten is favored for wall materials for next generation magnetic fusion devices. In D-T operation, significant He ash will be formed at 3.5 MeV, and its interaction with tungsten wall materials is currently undergoing extensive evaluation.

Under certain conditions of wall temperature and He fluence, He ions were found to cause significant morphology changes in the W surface [1-5], even for impact energies below the physical sputtering threshold of ~200-300 eV. While still not completely understood, such surface changes are thought to result from near-surface He trapping at intrinsic or extrinsic defect sites. Due to favorable energetics, the trapped He atoms form clusters, which result in progressively higher lattice distortions, which relax by dislocation loop punching, producing He-filled cavities (bubbles) of increasing size.

These He bubbles can eventually burst at high sample temperatures where the tungsten has lower effective viscosity or yield strength, causing surface pinholes, and eventually evolving into an increasingly random nanostructuring of the surface that can ultimately lead to the production of nano-fuzz [6-9]. There is concern that such surface nanostructuring may adversely affect the robustness of the W surface in the presence of the high-power fusion plasma due to increased W dust formation, as well as affect H and He retention. In addition, the effect of the material damage due to 14.1 MeV neutrons also produced in the D-T fusion reactions on these near surface He-W interactions has yet to be definitely assessed.

In this article we outline our measurements of interactions of 50 – 12,000 eV He ions with heated polished tungsten surfaces performed at the ORNL MIRF. Surface morphology changes, as well as nanofuzz formation were investigated as function of beam flux, fluence, and energy, as well as target temperature, for both virgin and pre-damaged W-targets. At low fluences, ordered coral-like and ridge-like surface structures are observed, with great grain-to-grain variability. At larger fluences, individual grain characteristics disappear, and the entire surface assumes a frothy appearance in FIB/SEM, with a multitude of near-surface bubbles with a broad range of sizes, and disordered whisker growth, while in SEM imaging the surface is indistinguishable from nano-fuzz produced on linear plasma devices. These features are evident at progressively lower fluences as the He-ion energy is increased. We also report on observations of the effects on surface-morphology changes and nanofuzz formation of pre-damage created by self-ion impact, and on MD simulations of near-surface damage using self-atoms. The self-ions or -atoms of suitable impact energies represent the Primary Knock-on Atoms (PKO) created by impacting neutrons in a burning fusion reactor that start the damage cascades in the first wall of magnetic fusion devices. Plasma-interface interactions in neutron-damaged wall materials have been relatively unexplored to date. In particular, the effects of near-surface radiation damage on nanofuzz formation still remain to be elucidated.

2. Experimental Approach

The measurements were carried out at the ORNL Multicharged Ion Research Facility [10] using a new beamline-deceleration module [11] capable of delivering high-current He ion beams at impact energies as low as 50 eV, and a new beam-profile-mapping device [12] that permits determination of detailed flux distributions of the ion beams impacting the tungsten samples.

Figure 1 shows typical flux profiles for decelerated and undecelerated He ion beams in the plane of

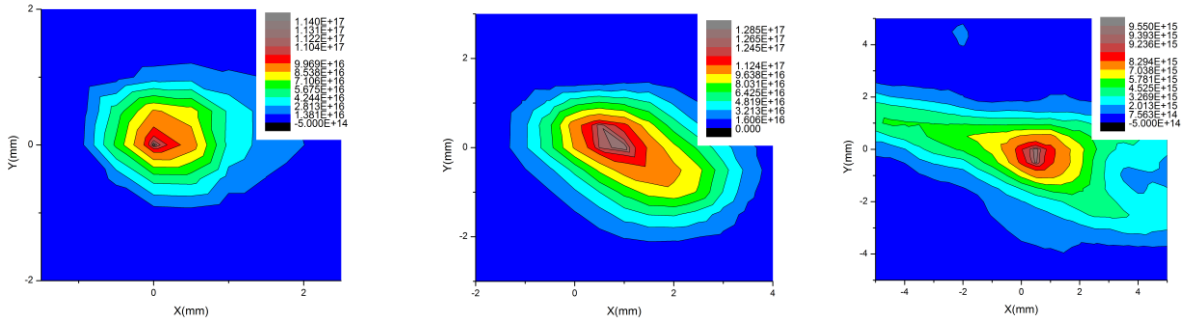

Figure 1- 2-D He ion beam flux profiles at (left to right) 10 keV, 1 keV, and 80 eV final beam energies; peak fluxes exceed 10^{17}/cm^{2}s above 1 keV He ion energy, and are still about 10^{16}/cm^{2}s at 80 eV.

the tungsten sample. He fluxes in excess of 10^{17}/cm^{2}s were obtained at energies of 1 keV and above, and of ~10^{16}/cm^{2}s at the lowest decelerated energies of 50 eV. With knowledge of the detailed flux distributions, flux dependences of nano-structuring and nanofuzz formation can in principle be measured in a single ion beam exposure. Figure 2 shows details of the flux profile cup, featuring a 1 mm square aperture that is scanned under computer control across the beam, and showing its location immediately below the tungsten sample. Since it is rigidly attached to the W sample holder, and the

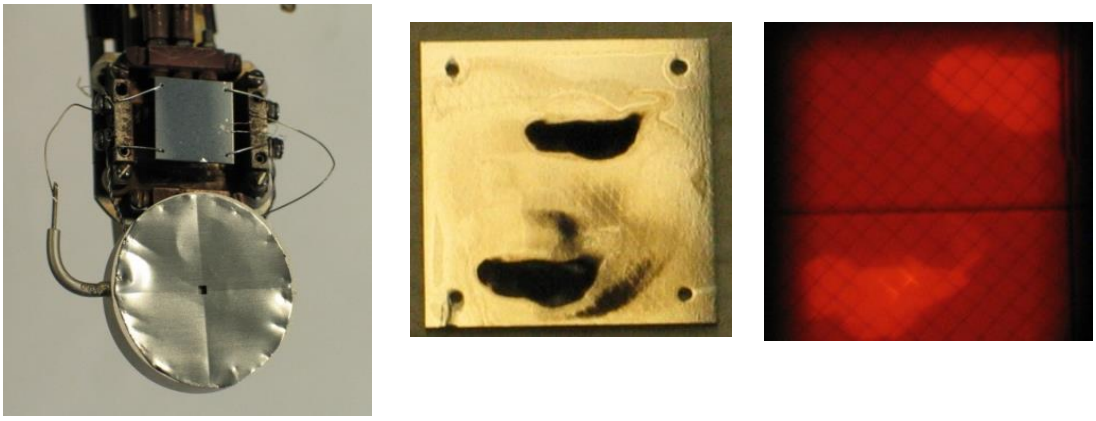

Figure 2 – (left) Beam profile mapping cup assembly and location below the 13x13 mm^2 tungsten sample. Note the 1 mm square cup entrance aperture in center of entrance diaphragm. Total current to the diaphragm as well as the suppressed inside current are monitored during the 2-D profile scans to monitor beam fluctuations. (center) W sample after 2 high-energy He ion beam exposures, showing black appearance of nanofuzz. (right) *In-situ* sample view through analyzing magnet view port during exposure of lower target spot at T~1200 K. The emissivity change due to nanofuzz formation affects sample temperature and makes IR optical pyrometry problematical. The 0.03 mm diameter wire, 92 % transmission W grid visible in photo is ~ 1 mm in front of sample, and is at same potential as sample; note grid incandescence due to beam heating on lower spot.

relative offsets between sample and cup are known, the measured spatial profile determined using the small aperture cup is straightforwardly mapped onto the beam exposed tungsten sample.

For the self-ion damage exposures, 30 keV W^{3+} ions were employed, and their beam flux profiles in the sample plane were determined in a similar manner. With exposures of about 2 hours, near–surface damage doses in excess of 50 dpa could be achieved [9].

The tungsten sample could be e-beam heated from the rear to temperatures up to 1650 K, as monitored by a 0.15 mm diameter chromel-constantan thermocouple. The sample temperature was monitored dynamically, i.e. during He ion beam exposure, since sample heating due to the beam itself was significant at some energies.

3. Representative Results

3.1 Experiment

Some representative experimental results are now presented. A more complete summary is reported in Ref. [9]. Figure 3 illustrates tungsten surface morphology changes at a sample temperature of 1400 K induced by 80 eV He ion impact at a flux of ~10^{16}/cm^2s to a fluence in excess of 5x10^{20}/cm^2. Under

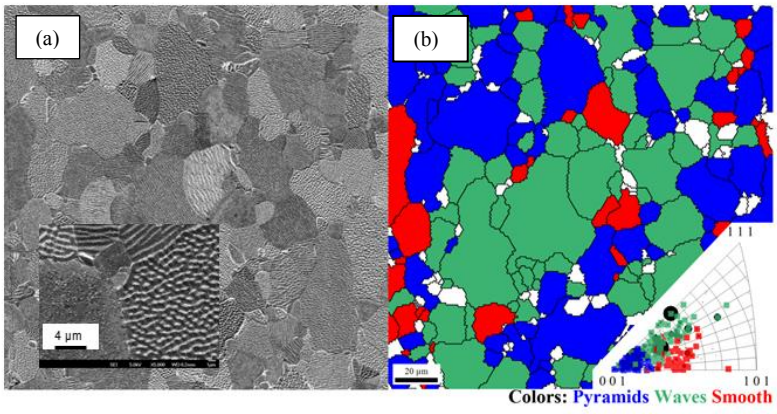

Figure 3 – (a) SEM's of W surface after He ion exposure under conditions described in text; note distinct grain features and their grain-to-grain variation; (b) electron back-scatter diffraction (EBSD) analysis of crystallographic orientation of 3 different observed features; note clustering of the different features in the inverse pole diagram shown in the inset.

these beam exposure conditions, ordered surface textural features become evident, which vary from grain to grain. Certain grains become either coral-like, pyramid-like, or sand-dune-like in appearance, while others maintain their original pristine flat appearance. It is important to realize that these surface morphology changes cannot be caused by ion-beam-induced lattice dislocations or surface-sputtering effects, since the ion energy is well below the respective threshold energies for these processes. Thus, these changes can only be due to built-up near-surface stresses [13] resulting from He implantation. Implanted He atoms trapped at near-surface intrinsic defects are highly effective at self-trapping additional He atoms [14], forming progressively larger He clusters [15]. The resulting lattice stresses are relieved by emission of self-interstitial atoms for small clusters and dislocation-loop punching as the cluster size increases. The resulting lattice relaxation progresses along preferred crystallographic directions, which may result in ordered surface-grain features such as seen in Figure 3a. Indeed, EBSD analysis has shown [16] that the type of feature evident for a particular surface grain is strongly

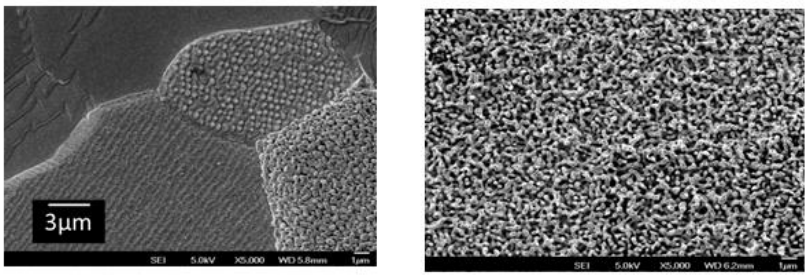

Figure 4 – W surfaces after exposure to 2 keV (left) and 10 keV (right) He ion beams with flux and fluence of 10^{17}/cm^{2}s and 5x10^{24}/cm^2, respectively, at 1400 K. Note transition from ordered features that preserve grain structure to disordered nanofuzz growth at right.

correlated with its crystallographic orientation, as can be seen from the close grouping of different individual surface features on an inverse pole diagram of the crystallographic orientation shown in the inset of Figure 3b.

At higher fluences and energies, disordered nanofuzz growth is induced by He-ion-beam exposure. The critical flux required for nanofuzz production appears to decrease with increasing energy. This trend is illustrated in Figure 4, which shows W surfaces after exposure by 2 and 10 keV He ion beams of roughly equal fluxes and fluences (~10^{17}/cm^{2}s and 5x10^{24}/cm^2, respectively) at sample temperatures of 1400 K. Both exposures shown in Figure 4 are carried out for He ion energies above the displacement damage threshold. Furthermore, both exposures were carried out to damage doses in excess of 100 dpa [9]. Due to their high fluxes, both He-beam exposures load the near-surface region of the W target with He to saturation, and at the same time produce significant near-surface damage sites that can trap He. This may lead to a supersaturation of the near-surface He concentration, particularly for the higher-energy He beam, with 3x higher damage dose [9]. It is speculated that this condition may initiate the disordered nano-fuzz growth evident in the 10 keV He ion exposure (see right SEM image in Figure 4).

We investigated the effect on surface-morphology changes of sample pre-damage by irradiating some tungsten samples with 30 keV W self-ions to damage doses in excess of 50 dpa, prior to exposure to high-flux and high-fluence He-ion beams. Figure 5 shows SEM images of the resulting surface morphologies for two different He ion energies. Interestingly, despite the high damage dose used for the pre-damage, only small changes were observed for the 80 eV He-ion exposure compared to what was observed using a virgin sample (see inset of Figure 3a). An increase in pinhole density in the ridge valleys is evident, but the original grain structure appears to be intact, i.e. no amorphization of the target has occurred. For the 12-keV He-ion exposure, a higher void density in the individual tendrils making up the nanofuzz growth is evident, but fuzz density appears unchanged. These relatively minor changes in surface morphology are at first surprising in view of the high damage doses presented. It should be kept in mind, however, that the self-damage and He exposures were done sequentially, leaving open the possibility of significant self-annealing prior to the He-ion-beam exposures.

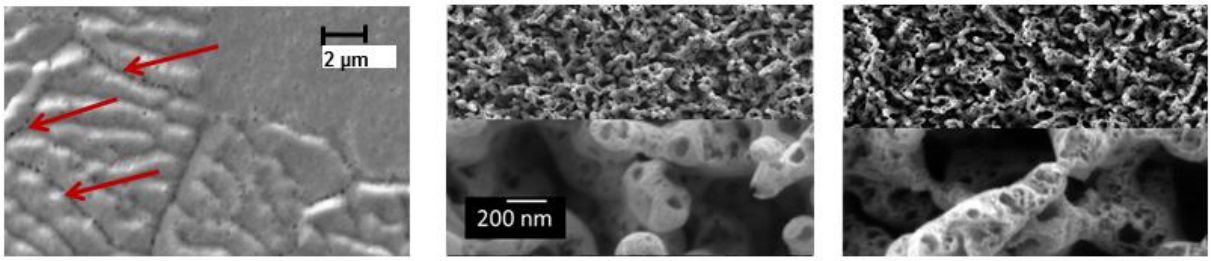

Figure 5 – Effect of W self-ion pre-damage on He-ion-induced surface-morphology changes: (Left) – 80 eV He exposure; increased pinhole density in valleys indicated by red arrows, but no amorphi-zation. (Right)- 12 keV He exposure; higher void density in tendrils compared to (center) - 12 keV He exposure of virgin W sample

In part to investigate this interesting possibility, we carried out damage simulations that account for the material response to the presented damage dose.

3.2 MD simulations

Using an extensive classical molecular dynamics (MD) calculation [9], the type, number, distribution, and evolution of defects were followed during cumulative bombardment by tungsten atoms of a 1000K tungsten surface. The initial (unperturbed) surface was modelled as a bcc tungsten lattice cube of

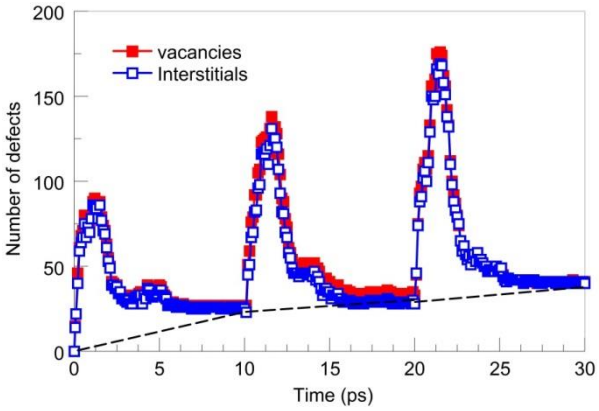

Figure 6- Formation and recombination of the defects in tungsten surface at 1000K simulated by 2D periodic cell of about 26,000 atoms, upon cumulative bombardment by 1 keV tungsten atoms. Time evolution of vacancies and interstitials is shown for the first three impacts. Recombination reduces the number of defects multiple times.

approximately 75 Å lateral dimension, containing more than 26,000 atoms, to which 2-D periodic boundary conditions were applied in the plane of the (100) surface-vacuum interface. The two bottom layers of the surface were "frozen", in order to prevent motion of the surface as a whole upon bombardment. The normally incident, 1 keV W atoms were launched at 15 ps intervals from a plane 15 Å above the surface, so as to impact the simulation cell at random positions.

As seen in Figure 6, following each W atom impact, an initial "blooming" of a large number of interstitials and vacancies occurs. With increasing time after impact, the cascade cools, and the number of defects stabilizes due to recombination of the vacancies with interstitials and implants, reaching a low, steady-state value in less than 10 ps. In the next 4 ps we apply a Langevin thermostat to all atoms of the surface in order to remove the deposited energy from the surface due to the most recent impact, and to return the surface temperature to 1000K. After additional 1 ps of system relaxation, the state of the simulation cell is queried and the results tabulated, as in Figure 7, after which a new W atom impact occurs. In the 15 ps time interval, all sputtered and reflected atoms have left the computational volume through an absorbing surface about 25 Å above the interface. This process is repeated 888 times, with a total elapsed time of more than 13 ns.

For the MD calculation we use the Large-scale Atomic/Molecular Massively Parallel Simulator (LAMMPS)[17], developed at Sandia National Laboratory, with a bond-order, Tersoff-type [18] tungsten interatomic potential (BOP) [19]. Though there are no chemical reactions in the considered

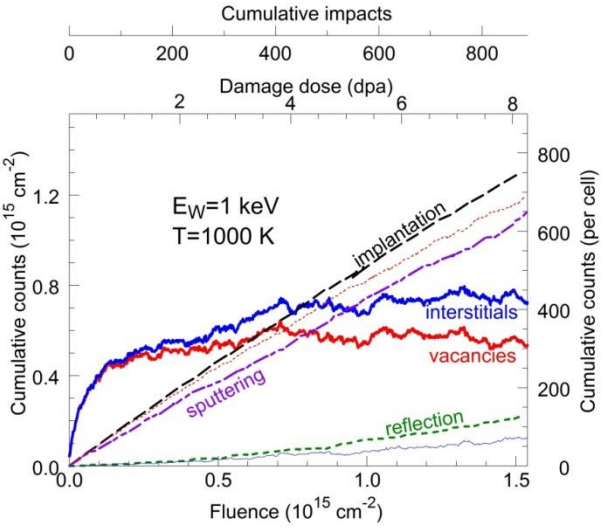

Figure 7 - Defect production by cumulative bombardment with 1 keV W atoms of a single-crystal tungsten surface described in Fig. 6 caption. Both vacancies and interstitials are shown after recombination takes place at each impact (dashed line in Fig. 1). Their numbers start saturating after about 100 impacts, i.e. at fluence of about $2\text{x}10^{14}$ or about 1 dpa.

system, use of the BOP opens possibilities for future studies of chemically active mixtures of damaged tungsten with carbon, oxygen and hydrogen. We note that use of the more popular Embedded Atom Method (EAM and its extension MEAM, [20]) resulted in only slightly accelerated calculation time, and produced virtually identical results. The calculations were performed using 1200 cores of the Cray X5 computer (Kraken) of the National Center for Computer Sciences of the University of Tennessee, and takes about 30 mins to follow the evolution of each impact for 15 ps.

Both implantation and sputtering play important roles in the final balance of the defects. Thus, the difference of interstitials and vacancies is equal to the difference of implanted and sputtered atoms; the thin red-dotted line in Figure 7 denotes the implants ending up and recombining at vacancy sites, while the thin blue line represents the implants ending up as interstitials. An excellent analytical fit to the saturated vacancy count, N_v, is given in terms of the number of impacts, k. It is interesting to discuss the irradiation flux of impinging atoms in the simulation. Although it is about 10^{26} cm^{-2}s^{-1} with impacts in 15 ps steps, the effective flux could be considered significantly smaller due to the fact that the system doesn't change after these 10-15 ps (Figure 6). The frequency of the impacts may even be a thousand times smaller, with most likely no change of results, before diffusion and other slow processes become important as times exceed the nanosecond scale, and result in further migration of the defects towards the interface or into the material bulk.

Sputtering, implantation and reflection remain linear functions of the impact number in the

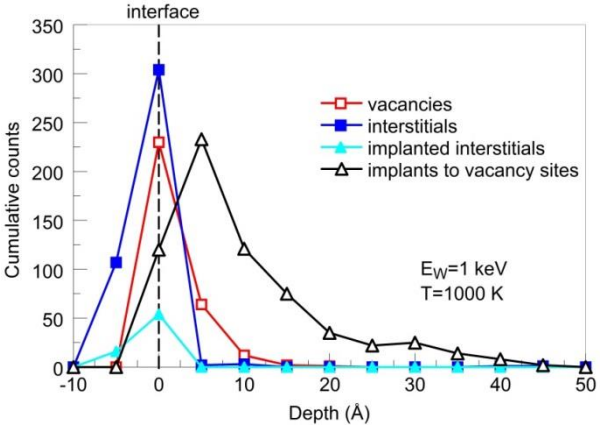

Figure 8- Illustration of the depth distribution of the cumulative defects from the surface interface (vertical dashed line) after 888 impacts. Most of the vacancies are distributed within 15 Å of the interface, since the deeper vacancies are filled by implanted atoms. Interstitials also occupy the 15 Å range, with the distribution extending about 5 Å above the interface, reflecting one aspect of surface roughening.

considered range of fluences. The efficiency of implantation is more than 86% per impact atom, and most of the implanted atoms (~ 90%) end up at vacancy sites, thus reducing the total number of vacancies remaining after the cool-down of each cascade in comparison to that deduced from the steady-state Frenkel pair count. The competing process, i.e. sputtering, is somewhat less efficient than implantation (about 72% per impact atom) at 1 keV impact energy. Sputtering produces vacancies, but in fewer numbers than their reduction due to implants that end up at vacancy sites. The difference of the number of interstitials and vacancies in Fig. 7 almost exactly reproduces the difference of implantation and sputtering counts. Particle reflection is low (below 15% per impact atom), though it gradually increases with impact number as the surface interface becomes "rougher" or "bumpier", due to the accumulated defects there. Finally, the implanted atoms contribute with less than 7 % to the interstitial defects. The dpa values shown in Figure 7 were deduced using SRIM [21] and the simulation fluences, using the procedure recommended by Stoller et al [22].

The depth distribution of defects experiences a statistical variation from impact to impact. However, in all cases most of the impacts are accumulated close to the surface-vacuum interface, reflecting damage of the first few layers of the surface. As illustration, we show in Figure 8 the distributions after the last considered impact (#888), corresponding to a fluence of $1.5x10^{15}/cm^2$, and a damage dose of more than 8 dpa (see Figure 6), by recording defects in 5Å bins, above and below the interface. The vacancy distribution extends to about 10 Å (~6 unperturbed atomic layers or lattice planes) in depth and is strongly peaked at the first bin. Significant numbers of interstitials accumulate above the original interface, ending up as much as 5 Å above the original surface. These adatoms together with vacancies in the first lattice plane result in surface roughening, and thus do not serve as He trapping sites. A more detailed analysis of the fraction of damage going into surface roughening versus that going into sub-surface defect production at this energy (that can serve as He trap sites) would be of great interest, and is planned using reduced bin widths that include just a single lattice plane, instead of the 3 encompassed in the bin widths reported here. Interestingly, vacancies initially created deeper in the bulk as steady-state Frenkel pairs are preferentially filled by implants. Thus, implantation causes narrowing of the vacancy distribution toward the surface.

4. Discussion

From the MD simulation results above, it is evident that, unlike the damage dose determined from SRIM, which is linear in accumulated fluence, the self-ion damage introduced quickly saturates as a function of fluence, and thus reduces the defect density in the near-surface region where He can be trapped. The saturation is most likely due to recombination of vacancies and interstitials that lie within a critical distance of each other, as has been discussed in connection with H retention in W pre-damaged by MeV-energy W self-ions [22]. This saturation behavior is evident in MD simulations carried out at higher self-atom energies as well [9], and thus is expected to be relevant at the 30 keV self-ion energies used here. One crucial difference between the pre-damage produced by W self-ions and the damage induced during the high-energy He-ion exposures arises from the time lag and temperature cycling that separate it from the subsequent He-ion exposure, which can reduce the defect density yet further. The high spatial and temporal correlation of the damage produced during the high-energy He-ion exposure and implanted He may make it significantly more effective in modifying surface morphology due to He cluster/bubble formation. These correlations could be improved by implementing co-irradiation of W self-ions and He ions. The feasibility of carrying this out experimentally is being currently investigated.

Acknowledgements

This research was sponsored by the LDRD Program of Oak Ridge National Laboratory, managed by UT-Battelle, LLC, for the U.S. Department of Energy. HH was appointed through the ORNL Postdoctoral Research Associates Program administered jointly by Oak Ridge Institute of Science and Education (ORISE), Oak Ridge Associated Universities (ORAU) and Oak Ridge National Laboratory (ORNL). SEM and FIB/SEM instruments supported by Oak Ridge National Laboratory's Shared

Research Equipment (ShaRE) User Program, which is sponsored by the Office of Basic Energy Sciences, U.S. Department of Energy. PSK and MJD acknowledge allocation of advanced computing resources provided by the National Science Foundation. The computations were performed on Kraken at the National Institute for Computational Sciences.

References

[1] Iwakiri H, Yasunaga K, Morishita K, Yoshida N, (2000) Journal of Nuclear Materials **283,** 1134-1138.
[2] Minyou Y, (2005) Plasma Science and Technology 7, 2828-2834.
[3] Nishijima D, Ye M Y, Ohno N, Takamura S, (2003) Journal of Nuclear Materials **313,** 97-101.
[4] Baldwin M J, Lynch T C, Doerner R D, Yu J H, (2011) Journal of Nuclear Materials **415,** S104-S107.
[5] Yamagiwa M, Kajita S, Ohno N, Takagi M, Yoshida N, Yoshihara R, Sakaguchi W, Kurishita H, (2011) Journal of Nuclear Materials **417**, 499-503.
[6] Baldwin M J, Doerner R P, (2008) Nuclear Fusion **48**, 035001.
[7] Baldwin M J, Doerner R P, (2010) J. Nucl. Mat. **404**, 165-173.
[8] Takamura S, Ohno N, Nishijima D, Kajita S, (2006) Plasma and Fusion Research **1**, 051.
[9] Meyer F W, Hijazi H, Krstic P S, Dadras S, Meyer III H M, Parish C M, Bannister M E, Physica Scripta, accepted for publication, Physica Scripta, 2013.
[10] Meyer M F, Bannister M E, Hale J W, Havener C C, Krause H F, Vane V R, Deng S, Draganic I N, Harris P R, Recent activities at the ORNL multicharged ion research facility (MIRF), Proceedings of ECRIS2010, Grenoble, France, http://accelconf.web.cern.ch/AccelConf/ECRIS2010/papers/mocobk04.pdf
[11] Hijazi H, Meyer F W, A large-acceptance beam-deceleration module for retrofitting into ion-source beam lines, (2013) Review of Scientific Instruments **84**, 033305.
[12] Bannister M E, Hijazi H, Meyer III H M, Cianciolo V, Meyer F W, Surface-conductivity enhancement of PMMA by keV-energy metal-ion implantation, Nuclear Instruments in Physics Research B, (Submitted).
[13] Evans J H, The Role of implanted gas and lateral stresses in blister formation, (1978) J. Nuc. Mat. **76-77**, 228.
[14] Baskes M I, and Wilson W D, (1983) Phys. Rev. **B27**, 2210.
[15] Henriksson K O E, Nordlund K, Keinonen J, (2006) Nucl. Inst. Meth. Phys. Res. **B 244**, 377.
[16] Parish C M, Hijazi H, Meyer III H M, and Meyer F W, Effect of tungsten crystallographic orientation on He-ion-induced surface morphology changes, submitted (Aug. 2013).
[17] Plimpton S, Fast Parallel Algorithms for Short-Range Molecular Dynamics, (1995) J. Comp. Phys. **117**, 1-19.
[18] Tersoff J, (1988) Phys. Rev. **B 37**, 6991.
[19] Juslin N, Erhart P, Traskelin P et al, (2005) J. Appl. Phys. **98**, 123520.
[20] Moitra A, Kim S, Houze J et al, (2008) J. Phys. D: Appl. Phys. **41**, 185406.
[21] Ziegler J F, Biersack J P and Littmark U, "The Stopping and Range of Ions in Solids", Pergamon Press, New York, 1985; http://www.srim.org/
[22] Stoller R E, Toloczko M B, Wasc G S et al, (2013) Nuclear Instruments and Methods in Physics Research **B 310**, 75.
[23] 't Hoen M H J, Tyburska-Püschel B, Ert K, Mayer M, Rapp J, Kleyn A W, and Zeijlmans van Emmichoven P A, (2012) Nucl. Fusion **52**, 023008.